The International Archives of the Photogrammetry, Remote Sensing and Spatial Information Sciences, Volume XLVIII-M-6-2025
ISPRS, EARSeL & DGPF Joint Istanbul Workshop “Topographic Mapping from Space” dedicated to Dr. Karsten Jacobsen’s 80th Birthday
29–31 January 2025, Istanbul, Türkiye

Machine Learning-Based Supervised Classification of Sentinel-2 MSI and Landsat-8 OLI Imagery in Marguerite Bay of Antarctic Peninsula

Mehmet Arkalı [1], Muhammed Enes Atik [1], Şaziye Özge Atik [1]

[1] ITU, Department of Geomatics Engineering, Civil Engineering Faculty, 34469 Maslak Istanbul, Türkiye – markali@itu.edu.tr; atikm@itu.edu.tr; donmezsaz@itu.edu.tr

Keywords: Antarctica, Machine Learning, Sentinel-2, Landsat-8, Object-based Classification, Pixel-based Classification.

Abstract

Especially in the last decade, many innovative advantages of machine learning algorithms have been known, and their use in places where the effects of climate change are closely monitored, such as the polar regions, has introduced revolutionary scientific breakthroughs. In this study, machine learning methods were used to classify Sentinel-2A and Landsat-8 OLI satellite images of Marguerite Bay of Antarctic Peninsula. Four supervised classification algorithms were applied for pixel-based and object-based classification. Random Forest (RF), Decision Tree (DT), Support Vector Machines (SVM), k-nearest neighbor (kNN) are the algorithms selected for object-based image analysis (OBIA). SVM, RF, Light Gradient Boosting Machine (LightGBM) and Extreme Gradient Boosting (XGBoost) were used for pixel-based classification. Each image is labelled into three classes: glacier, water and soil. The classification methods were analysed comparatively for each data set. In both Sentinel-2 and Landsat-8 images, 97.31% and 96.28% overall accuracy were achieved with SVM, respectively.

1. Introduction

Antarctica's ecosystem records atmospheric events from the past to the present. It offers the best environment for scientific studies aimed at monitoring the effects of global warming. Global warming, also known as the greenhouse effect, refers to the increase in the Earth's average surface temperature due to greenhouse gases trapping solar heat in the atmosphere. This effect occurs when greenhouse gases in the atmosphere absorb thermal radiation emitted from the Earth's surface, acting as a blanket over the surface (Houghton, 2005).

The cryosphere consists of areas of snow or ice exposed to temperatures below 0°C for at least part of the year. Glaciers, also a cryosphere component, hold more than 70% of the world's freshwater reserves. The largest parts of the cryosphere are located in Greenland and Antarctica. The Antarctic ice sheet contains approximately 91% of the world's ice (Baumhoer et al., 2018). Due to this feature, it is an important research area to examine the changes in glacier areas caused by global warming. Satellite remote sensing has facilitated significant advancements in comprehending the climate system and its changes by quantifying the processes and spatiotemporal states of the atmosphere, land, and oceans (Yang et al., 2013). Remote sensing allows the examination of characteristics and phenomena that are difficult to access or suitable for direct observation. Remote sensing satellites with many different sensors and measurement techniques are important for monitoring changes in glacial areas. Detecting changes in glacier areas contributes to future scientific studies by characterizing glacier balance and modelling climatic behaviour. The study involved using Sentinel-2 and Landsat-8 satellite images to perform feature extraction with classification in glacier fields. Satellite data were selected in February and March 2024. The selection of these dates considered important criteria, including the summer season in the southern hemisphere and the absence of cloud cover. Following the classification step, an accuracy assessment utilizing error matrices was used. The outcomes demonstrated that satellite data and pixel-based and object-based classification techniques were adequate for the classification of the region. Several machine learning algorithms are used for the classification: Random Forest (RF), Decision Tree (DT), Support Vector Machines (SVM), k-nearest neighbor (kNN), Light Gradient Boosting Machine (LightGBM), and Extreme Gradient Boosting (XGBoost). When used with the Sentinel-2 and Landsat-8 satellite images, the pixel-based classification conducting SVM algorithm also increased the classification accuracy.

2. Study Area and Data

The study area was chosen near Horseshoe Island and its surroundings, situated in the Marguerite Bay archipelago in the south-central portion of the Antarctic Peninsula (Figure 1). The total area of Horseshoe Island is approximately 60 km^2. In addition, Horseshoe Island serves as the Turkish base for the Turkish Science Expeditions in the Antarctic Continent. In the summer, water, glaciers, and soil areas are more visible in the study area than in winter.

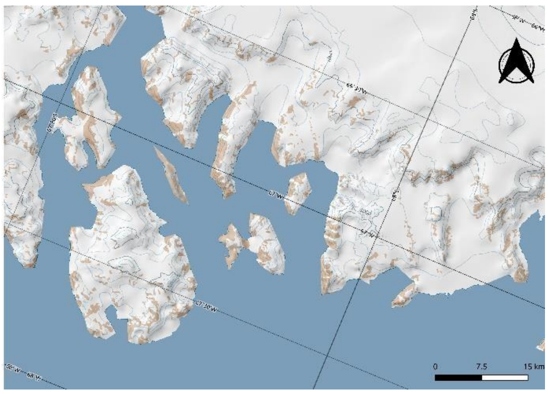

Figure 1. Study area. Marguerite Bay of Antarctica.

Landsat-8 was launched on February 11th, 2013. Landsat-8 data has been publicly accessible since May 2013. Landsat-8 satellite imagery ranges from 15m to 100m for spatial resolution up to the bands (Table 1). Landsat-8 has an Operational Land Imager (OLI) instrument, and the thermal bands 10 and 11 had a spatial resolution of 100 m, which had previously been reduced to 30 m by the data vendor, Earth Resources Observation and Science Center (EROS), United States Geological Survey (USGS).

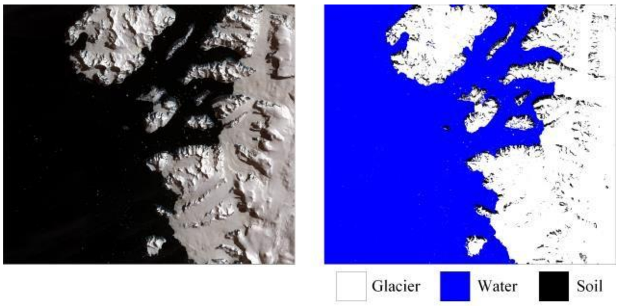

Figure 2. Landsat-8 OLI satellite image (left) and ground truth (right).

Band	Band Name	Wavelength (µm)	Resolution (m)
1	Coastal aerosol	0.43–0.45	30
2	Blue	0.45–0.51	30
3	Green	0.53–0.59	30
4	Red	0.64–0.67	30
5	NIR	0.85–0.88	30
6	SWIR 1	1.57–1.65	30
7	SWIR 2	2.11–2.29	30
8	Panchromatic	0.50–0.68	15
9	Cirrus	1.36–1.38	30
10	Thermal Infrared 1	10.6–11.19	100*(30)
11	Thermal Infrared 2	11.50–12.51	100*(30)

Table 1. Landsat-8 OLI spectral bands.

OLI is a push-broom sensor featuring a four-mirror telescope and operates with 12-bit quantization. It gathers data across visible, near-infrared, and shortwave infrared spectral bands and a panchromatic band. In contrast, the OLI optical bands 2–7 had a spatial resolution of 30 m (Bhatti, 2014). There is a 15 m spatial resolution in panchromatic band 8. In the study, a 5-band stacked image is used for the classification using 30m spatial resolution bands of Blue, Green, Red, NIR, and NDWI layers. It uses more bands than RGB bands because its more effective feature extraction is the aim. In general, algorithms perform better as the number of bands rises (Atik, 2024). In the study, the Landsat-8 OLI image was used; the acquisition date is February 4th, 2024.

Launched on June 23rd, 2015, the Sentinel-2 mission provides global optical imagery. Sentinel-2 collects multispectral data in 13 bands in the spectrum's visible, near-infrared, and shortwave infrared regions. Table 2 displays the wavelength range, spatial resolution, and band names of Sentinel-2A. It has an MSI (Multispectral Imager) sensor for satellites Sentinel 2A, 2B, and 2C. In the study, Sentinel-2A image was used; the acquisition date is March 15th, 2024.

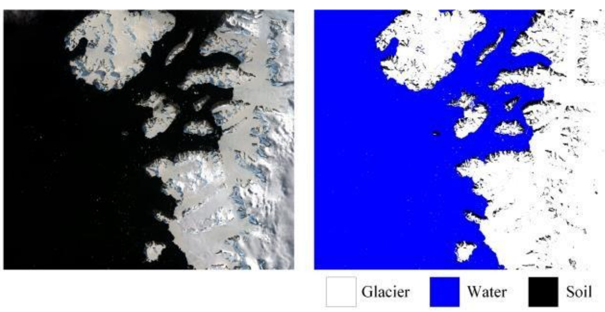

Figure 3. Sentinel 2A satellite image (left) and ground truth (right).

Band	Band Name	Wavelength (µm)	Resolution (m)
1	Coastal aerosol	0.43–0.45	60
2	Blue	0.46–0.52	10
3	Green	0.54–0.58	10
4	Red	0.65–0.68	10
5	Vegatation Red Edge	0.70–0.71	20
6	Vegatation Red Edge	0.73–0.75	20
7	Vegatation Red Edge	0.77–0.79	20
8	NIR	0.78–0.90	10
8a	NIR	0.85–0.87	20
9	Water Vapor	0.93–0.95	60
10	SWIR Cirrus	1.36–1.39	60
11	SWIR	1.56–1.65	20
12	SWIR	2.10–2.28	20

Table 2. Sentinel-2A spectral bands.

The weather conditions present during the data collection period for this study were thoroughly considered to enhance the validity of our findings (Figure 4). This is emphasized in order to optimize the parameters affecting the classification performance. It was observed that the temperature was approximately 0 °C in both months, and the amount of precipitation decreased.

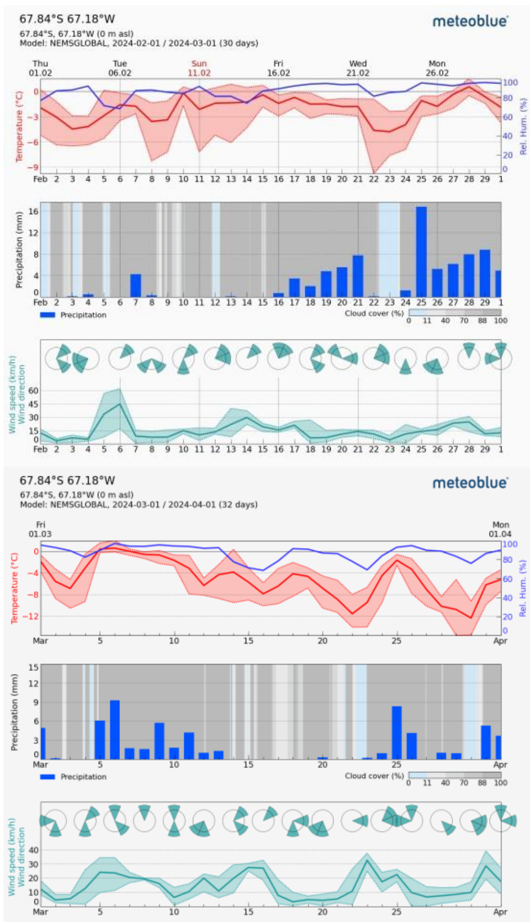

Figure 4. Weather conditions for the study period (URL-1).

3. Methods

Two different supervised classification methods are used in this study: pixel-based and object-based. Object-based classification is a more complex process but can be advantageous, especially when using high-spatial resolution imagery. It is also used to reduce the salt-pepper effect on the classification images.

However, pixel-based classification is still the most popular method when using lower or medium-spatial-resolution images.

Object-based image analysis (OBIA) and pixel-based classification are the main classification techniques. In contrast to pixel-based classification, which employs the spectral information of each pixel inside the study area object-based classification considers other factors, such as spatial, textual, or contextual information (Gavankar and Ghosh, 2019). This makes the object-based approach seem more sophisticated (Isiler et al., 2023). The segmentation stage is essential for grouping related pixels. According on geometrical, topological, and/or textural features, image segmentation suggests extracting segments as spatially and spectrally grouped pixels. Additionally, the OBIA professional modifies the segmentation parameters according to the application (Atik et al., 2018; Schöpfer et al., 2010). In the study, multi-resolution segmentation (MRS) algorithm is chosen for segmentation phase. After segmentation, machine learning classifiers were re-conducted for the data. In Landsat-8 image scale parameter is 75 and the shape is selected as 0.2. On the other hand, for the Sentinel-2 dataset, the scale parameter is conducted as 65, and the shape parameter is selected as 0.1.

In the study, one of the most popular spectral indices is selected for band stacking to extract water effectively. The NDWI is a spectral index that improves the visibility of open water bodies in digitally captured images from remote sensing while also eliminating elements of soil and land vegetation (McFeeters, 1996; Singh et al., 2018; Singh and Kansal, 2022). The NDWI calculation has utilized Green and Near-Infrared (NIR) bands (1).

$$\mathrm{NDWI} = \frac{\mathrm{Green} - \mathrm{NIR}}{\mathrm{Green} + \mathrm{NIR}} \tag{1}$$

For Landsat-8, the NDWI equation (2) is expressed in the following manner:

$$\mathrm{NDWI} = \frac{\mathrm{Band\ 3} - \mathrm{Band\ 5}}{\mathrm{Band\ 3} + \mathrm{Band\ 5}} \tag{2}$$

For Sentinel-2, the equation (3) for NDWI can be represented as follows:

$$\mathrm{NDWI} = \frac{\mathrm{Band\ 3} - \mathrm{Band\ 8}}{\mathrm{Band\ 3} + \mathrm{Band\ 8}} \tag{3}$$

The objective of this research is to conduct a comparative analysis of the results obtained from controlled pixel-based classification and object-based classification methodologies. Different machine learning algorithms are chosen for this aim. Traditional supervised classification and unsupervised classification usually work based on predicting the label of a single pixel. In other words, the general goal of classification is to automatically detect the land cover and land use classes of all pixels in the image. Machine learning is a powerful mathematical tool for classifying remote sensing images. Instead of predefined parameters, machine learning algorithms automatically use training data to learn labeling criteria. For this purpose, machine learning provides classifiers with successful results (Atik et al., 2021).

3.1 Support Vector Machines (SVM)

SVM is a supervised machine learning algorithm applicable for classification and regression purposes (Cortes and Vapnik, 1995a). The optimal hyperplane is determined using equation (4) for a set of samples represented as $x_i (i = 1,2, \dots, N)$

$$f(x) = w^T x + b = \sum_{j=1}^{N} w_j x_j + b = 0 \tag{4}$$

Here, w denotes an N-dimensional vector and b is a scalar. Together they are used to define the hyperplane.

In the experiments, SVM algorithm is used for both classification types. In object-based classification the parameters are preferred as: kernel type is linear and C constant is equal to 2. The training parameters are selected as radial basis function (rbf) for kernel, 100 for C parameter and 100 for cache size in the pixel-based classification.

3.2 K-nearest neighbor (kNN)

The conventional kNN algorithm represents one of the earliest and most straightforward approaches to pattern classification. Being a non-parametric approach, it does not depend on a preestablished model, which places it in the category of instancebased or lazy learning methods. The kNN algorithm classifies unlabeled data points by assigning the majority label from their k nearest neighbors (Sun and Huang, 2010). The influence of neighboring points is determined by their distance from the query point, with closer neighbors receiving higher weights due to an inverse proportionality to their distance. This algorithm is used only in object-based classification, and the k number is selected as 1.

3.3 Random Forest (RF)

An enhanced bagging technique called Random Forest (RF) generates a significant sample of uncorrelated trees and then averages them (Breiman, 2001a). Each random forest tree provides a class estimate, and the model predicts the class that receives the most votes. A training data set is allocated to each tree in the bagging technique, which creates several bootstrap training data sets from the initial training data set to train a classifier. The RF classifier requires two parameters to produce a tree. The parameters include the number of variables per node and the number of trees for optimal splitting. Boot samples are drawn from 2/3 of the training data, while the remaining 1/3, known as out-of-bag (OOB) data, is used to test errors. The resulting error is referred to as the generalized error. The computation of generalized error (PE) is illustrated in Equation (5):

$$PE^* = P_{X,Y}(mg(X,Y) < 0) \tag{5}$$

The term $mg()$ denotes the margin function. The margin quantifies the extent to which the mean vote counts in (X, Y) for the correct category surpasses the mean vote count for all other categories.

In the experiments, RF algorithm is preferred to be used in both classification implementations. Object-based classification parameters are chosen as follows: maximum tree numbers are 50, and forest accuracy parameter is equal to 0.01. In pixel-based classification, training parameters are 200, 10, 10, and 100 for the number of estimators, max_features, minimum sample split, and random state, respectively.

3.4 Extreme Gradient Boosting (XGBoost)

An efficient and scalable algorithm based on a gradient boosting tree, XGBoost, has been created as an effective technique for classification and regression problems (Chen and Guestrin, 2016a). With n samples and m features, the dataset $D = \{(x_i, y_i)\}$ is estimated using a tree ensemble model that employs

https://doi.org/10.5194/isprs-archives-XLVIII-M-6-2025-45-2025 |

functions of K additive. To calculate the prediction, use this formula:

$$\hat{y}_i = \emptyset(x_i) = \sum_{k=1}^{K} f_k(x_i), \quad f_k \in \varphi \tag{6}$$

$$\varphi = \{f(x) = \omega_{q(x)}\}(q: R^m \to T, \omega \in R^T, \tag{7}$$

Where $\hat{y}_i$ denotes the model's prediction [Eq. (6)], x_i is an observation, $f_k(x_i)$ and indicates the predicted score for the given observation. φ refers to the set of regression trees [Eq. (7)], with the independent tree structure q. T is the number of leaves on the tree, and their weights are ω_q (Atik and Atik, 2024).

The objective function of XGBoost [Eq. (8)] consists of two terms: the traditional loss function and the complexity of the model. To learn the set of functions used in the model, XGBoost aims to minimize the regularised objective function:

$$L(\emptyset) = \sum_{\mathrm{i}} l(\hat{y}_i, y_i) + \sum_k \Omega(f_k) \tag{8}$$

$$\Omega(f) = \gamma T + \frac{1}{2}\lambda\|\omega\|^2. \tag{9}$$

The differentiable convex loss function, which computes the difference between the target y_i and the prediction $\hat{y}_i$, is the first term in Eq. (8). Model complexity is penalized using the second term in Eq. (9). Tree complexity is adjusted using γ and λ. The extra regularization term prevents overfitting and smoothes the final learning weight. XGBoost algorithm is used for pixel-based classification process. Appropriate training parameters are max_depth=10, learning_rate=0.1 and n_estimators=200.

3.5 Light Gradient Boosting Machine (LightGBM)

A tree-based algorithm called LightGBM was created by Microsoft using the GBDT (gradient boosting decision tree) principle to solve prediction problems in massive, highdimensional data quickly and effectively. XGBoost has been improved upon by LightGBM (Ke et al., 2017). The gradientbased one-side sampling algorithm used by LightGBM allows for a fair balance between the DT's precision and sample size. LightGBM is applied when pixel-based classification in the study. The optimum training parameters are selected as num_leaves=10, max_depth=0.1, min_data_in_leaf=50, and n_estimators=200.

3.6 Decision Tree (DT)

Due to their non-parametric form and ease of interpretation, DTs have been applied to image-based classification. There are various implementations (Punia et al., 2011; Powers et al., 2015; Phiri et al., 2019), and it is one of the widely used machine learning algorithm in OBIA. Establishing decision rule sets is a crucial first step in the OBIA process for classifying land cover. However, this stage calls for class-related thresholds, which can be set using straightforward DTs or knowledge-based approaches. The knowledge-based strategy might get complicated when numerous land covers and decision variables are involved (Phiri et al., 2023). In object-based classification, geographic location, area, shape, topography, and temporal change features also can be used for implementing hierarchically DTs (Wang et al., 2023). This algorithm is assessed in the objectbased classification of the study. The value of maximum categories is 16, and cross-validation folds of 3 are chosen int assessing.

3.7 Evaluation Metrics

A confusion matrix is used to calculate the metric values that are obtained in machine learning. Eq. (10) – (13) present the metrics' equations.

$$Overall\ Accuracy = \frac{TP + TN}{TP + TN + FP + TN} \tag{10}$$

$$Precision\ (P) = \frac{TP}{TP + FP} \tag{11}$$

$$Recall\ (R) = \frac{TP}{TP + FN} \tag{12}$$

$$F1\ score\ (F1) = 2\frac{Precision \cdot Recall}{Precision + Recall} \tag{13}$$

The number of points that are positive predicted and actual label is known as the true positive (TP). The number of points that are predicted negative label and actually have a negative label is known as the true negative (TN). The number of points that are predicted as positive but are actually labeled as negative is known as a false positive (FP). The number of points that are expected to be labeled as negative but are actually labeled as positive is known as a false negative (FN) (Duran et. al., 2021).

4. Results and Discussion

OBIA was conducted for object-based classification using kNN, RF, DT, and SVM algorithms. In pixel-based classification, RF, SVM, XGBoost and LightGBM were employed to extract water, soil, and glacier classes.

In classification step, train samples are not used in test phase in all algorithms. The same ground truth image is conducted to all experiments and the same groups of samples are used for comparing inside object-based and pixel-based classification.

In this study SVM, kNN, RF, DT, XGBoost and LightGBM algorithms are applied as classifiers in classification of water, glacier and soil classes. In the Table 3, it is demonstrated that when comparing the results of pixel-based and object-based classification for both metric of overall accuracy and F1-score, SVM algorithm is superior to other classifiers in Sentinel-2A dataset. It is shown as percentage values in the Table 3-6. Overall accuracy is yielded as 97.31% and F1-score is obtained as 88.35%.

		Metrics	
Method	**Model**	**Accuracy**	**F1-score**
Pixel-based	SVM	**97.31**	**88.35**
	RF	97.01	88.09
	LightGBM	96.75	87.42
	XGBoost	97.09	88.04
OBIA	SVM	94.39	81.43
	RF	92.36	79.87
	kNN	92.51	79.33
	DT	92.52	79.84

Table 3. Classification results of Sentinel-2. All values are in %.

In Landsat-8 dataset, as similar SVM algorithm provided the best results regarding overall accuracy and F1-score metrics. However, a few decreases are observed due to spatial resolution being coarser in Landsat-8 than Sentinel-2. Overall accuracy is obtained as 96.28% when F1-score is 86.84% performance. When

https://doi.org/10.5194/isprs-archives-XLVIII-M-6-2025-45-2025 | © Author(s) 2025. CC BY 4.0 License.

comparing the algorithms inside the group of object-based classification, for Sentinel-2 image, SVM algorithm produced better results, and kNN algorithm provided higher performances than the others. These results differences are also related to algorithms' parameter optimization issue.

		Metrics	
Method	**Model**	**Accuracy**	**F1-score**
Pixel-based	SVM	**96.28**	**86.84**
	RF	95.46	86.06
	LightGBM	96.12	86.72
	XGBoost	95.77	86.64
OBIA	SVM	88.73	75.06
	RF	90.59	76.19
	kNN	91.87	78.41
	DT	90.59	75.92

Table 4. Classification results of Landsat-8. All values are in %.

The classification results are demonstrated in Figure 5-6. The blue color refers to the water class, black defines the soil class, and white refers to the glacier class. In Table 5-6, performance metrics are shown as class-based. According to Sentinel-2 dataset, mostly pixel-based classification provided the best results. However, there is no exact pattern that the same algorithm gave the same effect on the experiments by classbased. Also, pixel-based classification results were the best in the experiments with the Landsat-8 image. Again, we do not find a pattern about algorithms and repeated results for the different scenarios. We can interpret the results related to using middle spatial resolution imagery in the experiments. Pixel-based classification in machine learning classifiers performed better when compared to object-based classification. Therefore, in such as class level, these spatial resolutions of the data are proper to assess. In higher detail levels high high-resolution images can be preferred. However, medium-resolution images such as Landsat8 and Sentinel-2 are available for all users and have good temporal resolution. In Figure 3, in both pixel-based and objectbased classification results, it is seen that a small cloudy region on the upper left side is mixed with soil class for all algorithms for Sentinel image.

Furthermore, in Figure 4 for Landsat-8 image only OBIA implementation of SVM algorithm has a similar bias in the same region, but the reason is not about being cloudy. The parameters selected during the use of the SVM algorithm greatly affect the classification result. The appropriate selection of the C constant or the effect of the kernel type being linear or rbf directly affects the accuracy. Although the same parameters were selected for the SVM algorithm in the OBIA application in this study, the Landsat data did not yield as good results as the Sentinel data.

In general, on OBIA classification results more wider soil class is found when comparing pixel-based classification on the images. Therefore, in OBIA, although the recall metrics of the classes are high, the precision values are low. The classification of segments affects a group of pixels; classification algorithms are standard for each pixel of the segments, and decisions are made that affect the class to which they will be assigned. In addition, while applying OBIA algorithms, the training phase samples were also selected as segments. In this case, the presence of pixels in the sample segment that are incompatible with the assigned class may cause bias in the machine learning part of the algorithms. Therefore, when medium and low-resolution data are used, a product such as a mixed segment is assigned to a single class in OBIA results, which may negatively affect the accuracy. However, if the spatial resolution of the data used is high or very high, the probability of mixed segment decreases. The probability that all pixels in a class belong to the same class increases considerably. This does not reduce the accuracy in classification. In fact, it can be useful to eliminate the salt-pepper effect encountered in pixel-based classification. This study shows that pixel-based classification produces sufficient and successful results in medium-resolution data in the separation of classes at the basic level where different classifiers are used. Considering both the simplicity in the processing phase and the superiority of the results compared to OBIA, using machine learning algorithms to separate water, glacier and soil classes is beneficial for pixel-based classification.

5. Conclusion

Scientific studies have revealed that climate change is of great importance and is followed very closely. Global warming is a topic that can potentially affect the entire world, especially the polar regions. Therefore, with the technological developments, periodic monitoring of ice masses and surrounding classes is one of the hot topics. In this study, different combination of machine learning algorithms these are kNN, DT, RF, SVM, LightGBM and XGBoost were conducted to Landsat-8 and Sentinel-2 images in the Antarctic region. Additionally, to red, green, blue, and NIR bands, NDWI indices are added to the dataset of the study. In the means of overall accuracy and F1score metrics, pixel-based classification gave the superior results using SVM algorithm. In the future studies another spectral index for differentiating and extracting glacier class can be used for the satellite image of the same specifications. Such studies are of great importance and widely supported in serving the United Nations (UN) Sustainable Development Goals (SDGs), particularly Climate Action and Life on Land.Studies on the UN SDGs, such as technical monitoring and earth observation, are becoming more crucial (Atik and Ipbuker, 2022).

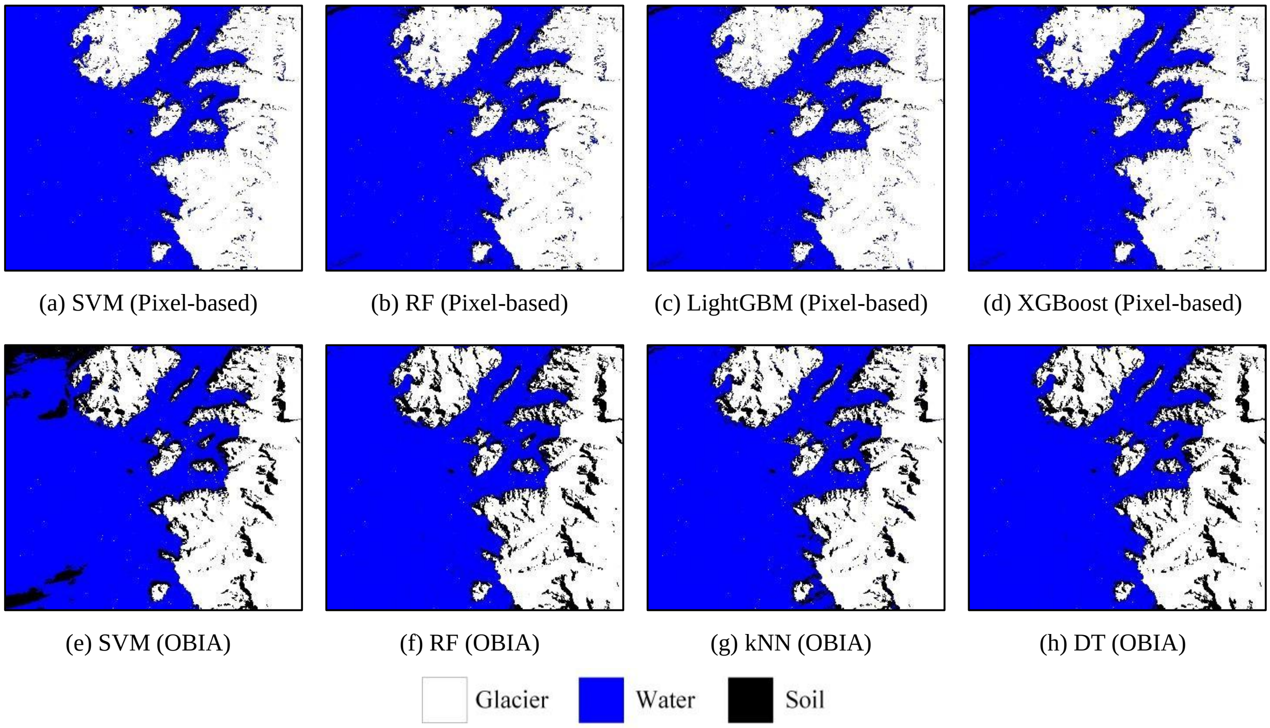

Figure 6. Classification results of Landsat-8.

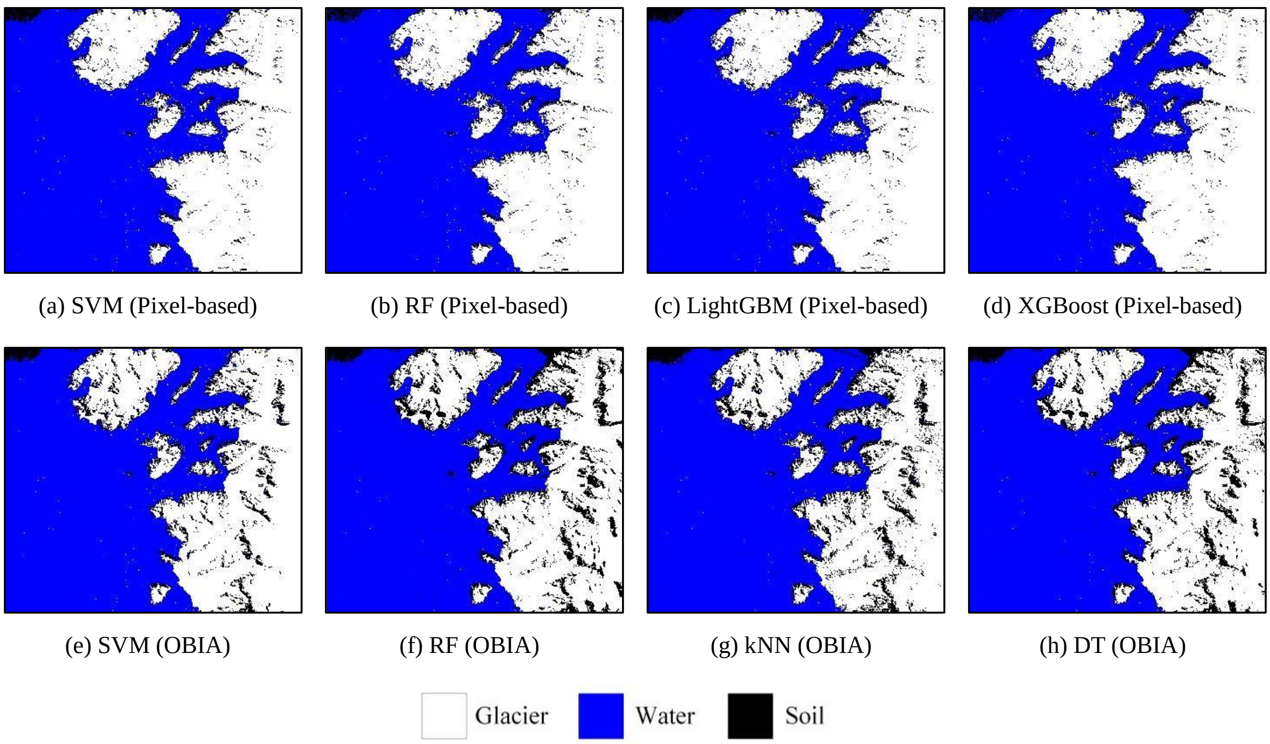

Figure 5. Classification results of Sentinel-2.

		Glacier			**Water**			**Soil**		
Method	**Model**	**P**	**R**	**F1**	**P**	**R**	**F1**	**P**	**R**	**F1**
	SVM	97.63	**98.75**	**98.19**	98.63	98.59	**98.61**	72.60	64.38	68.24
	RF	97.69	98.05	97.87	97.99	98.61	98.30	**73.13**	63.72	**68.10**
Pixelbased	LightGBM	97.78	97.54	97.66	98.06	98.39	98.22	67.12	65.62	66.36
	XGBoost	97.70	98.32	98.01	98.16	98.59	98.37	72.67	63.42	67.73
	SVM	97.87	91.28	94.46	98.47	**98.63**	98.55	41.04	68.34	51.29
	RF kNN	**99.21**	85.63	91.92	**99.75**	97.51	98.62	33.61	**90.78**	49.06
OBIA		98.34	86.87	92.25	99.25	97.59	98.41	33.46	80.85	47.33
	DT	98.81	86.43	92.21	**99.75**	97.45	98.59	33.76	87.44	48.71

Table 5. Class-based classification results of Sentine-2A. All values are in %.

		Glacier			**Water**			**Soil**		
Method	**Model**	**P**	**R**	**F1**	**P**	**R**	**F1**	**P**	**R**	**F1**
	SVM	97.87	95.74	**96.79**	96.57	**99.35**	97.94	**72.07**	60.54	65.80
	RF	97.49	94.60	96.02	96.39	98.21	97.29	63.43	66.40	64.88
Pixelbased	LightGBM	97.38	**95.90**	96.64	97.27	98.55	97.91	66.43	64.83	65.62
	XGBoost	97.17	95.18	96.17	96.43	98.57	97.49	69.70	63.16	**66.27**
	SVM	**98.49**	84.12	90.74	98.69	92.39	95.44	25.28	**85.17**	38.99
	RF kNN	98.46	81.06	88.92	**98.84**	98.50	98.67	27.70	78.61	40.97
OBIA		98.23	85.68	91.53	98.66	97.28	97.97	32.04	79.85	45.73
	DT	98.46	81.06	88.92	98.71	98.54	**98.63**	27.25	76.65	40.20

Table 6. Class-based classification results Landsat-8. All values are in %.

Acknowledgements

We want to thank the European Space Agency and Copernicus program management and staff, as well as the USGS Landsat program management and staff, for freely providing Sentinel-2A and Landsat-8 data, respectively.

References

Atik, S.O., 2024. Dual-Stream Spectral-Spatial Convolutional Neural Network for Hyperspectral Image Classification and Optimal Band Selection. *Advances in Space Research*, 74, 2025–2041. doi.org/10.1016/j.asr.2024.05.064.

Atik, M.E., Donmez, S.O., Duran, Z., İpbüker, C., 2018. Comparison of automatic feature extraction methods for building roof planes by using airborne lidar data and high resolution satellite image. *Proceedings Book of ICCGIS*.

Atik, M.E., Duran, Z., Seker, D.Z., 2021. Machine Learning-Based Supervised Classification of Point Clouds Using Multiscale Geometric Features. *ISPRS International Journal of Geo-Information*, 10, 187. doi.org/10.3390/ijgi10030187.

Atik, S.O., Atik, M.E., 2024. Optimal band selection using explainable artificial intelligence for machine learning-based hyperspectral image classification. *JARS*, 18, 042604. doi.org/10.1117/1.JRS.18.042604.

Atik, S.O., Ipbuker, C. 2022. Building Extraction in VHR Remote Sensing Imagery Through Deep Learning. *Fresenius Environ. Bull*, 31, 8468-8473.

Breiman, L., 2001a. Random Forests. *Machine Learning*, 45, 5–32. doi.org/10.1023/A:1010933404324.

Breiman, L., 2001b. Random Forests. *Machine Learning*, 45, 5–32. doi.org/10.1023/A:1010933404324.

Chen, T., Guestrin, C., 2016a. XGBoost: A Scalable Tree Boosting System. *Proceedings of the 22nd ACM SIGKDD International Conference on Knowledge Discovery and Data Mining. Presented at the KDD ’16: The 22nd ACM SIGKDD International Conference on Knowledge Discovery and Data Mining*, ACM, San Francisco California USA, 785–794. doi.org/10.1145/2939672.2939785.

Chen, T., Guestrin, C., 2016b. XGBoost: A Scalable Tree Boosting System. *Proceedings of the 22nd ACM SIGKDD International Conference on Knowledge Discovery and Data Mining, KDD ’16. Association for Computing Machinery*, New York, NY, USA, 785–794. doi.org/10.1145/2939672.2939785.

Cortes, C., Vapnik, V., 1995a. Support-vector networks. *Mach Learn*, 20, 273–297. doi.org/10.1007/BF00994018.

Cortes, C., Vapnik, V., 1995b. Support-vector networks. *Mach Learn*, 20, 273–297. doi.org/10.1007/BF00994018.

Duran, Z., Ozcan, K., Atik, M.E., 2021. Classification of Photogrammetric and Airborne LiDAR Point Clouds Using Machine Learning Algorithms. *Drones,* 5, 104. doi.org/10.3390/drones5040104.

Gavankar, N.L., Ghosh, S.K., 2019. Object based building footprint detection from high resolution multispectral satellite image using K-means clustering algorithm and shape parameters. *Geocarto International*, 34, 626–643. doi.org/10.1080/10106049.2018.1425736.

Isiler, M., Yanalak, M., Atik, M.E., Atik, S.O., Duran, Z., 2023. A Semi-Automated Two-Step Building Stock Monitoring Methodology for Supporting Immediate Solutions in Urban Issues. *Sustainability*, 15, 8979. doi.org/10.3390/su15118979.

Ke, G., Meng, Q., Finley, T., Wang, T., Chen, W., Ma, W., Ye, Q., Liu, T.-Y., 2017. LightGBM: A Highly Efficient Gradient Boosting Decision Tree. *Advances in Neural Information Processing Systems*. Curran Associates, Inc.

McFeeters, S.K., 1996. The use of the Normalized Difference Water Index (NDWI) in the delineation of open water features. International Journal of Remote Sensing, 17, 1425–1432. doi.org/10.1080/01431169608948714.

Singh, S., Dhasmana, M.K., Shrivastava, V., Sharma, V., Pokhriyal, N., Thakur, P.K., Aggarwal, S.P., Nikam, B.R., Garg, V., Chouksey, A., Dhote, P.R., 2018. Estimation of Revised Capacity in Gobind Sagar Reservoir Using Google Earth Engine and GIS. *The International Archives of the Photogrammetry, Remote Sensing and Spatial Information Sciences*, XLII–5, 589–595. doi.org/10.5194/isprs-archives-XLII-5-589-2018

Singh, S., Kansal, M.L., 2022. Chamoli flash-flood mapping and evaluation with a supervised classifier and NDWI thresholding using Sentinel-2 optical data in Google earth engine. *Earth Sci Inform*, 15, 1073–1086. doi.org/10.1007/s12145-022-00786-8.

Sun, S., Huang, R., 2010. An adaptive k-nearest neighbor algorithm, in: 2010 Seventh International Conference on Fuzzy Systems and Knowledge Discovery. *Presented at the 2010 Seventh International Conference on Fuzzy Systems and Knowledge Discovery*, 91–94. doi.org/10.1109/FSKD.2010.5569740.

Punia, M., Joshi, P., Porwal, M., 2011. Decision tree classification of land use land cover for Delhi, India using IRS-P6 AWiFS data. *Expert Syst. Appl.*, 38, 5577–5583.

Powers, R.P., Hermosilla, T., Coops, N.C., Chen, G., 2015. Remote sensing and object-based techniques for mapping fine-scale industrial disturbances. *Int. J. Appl. Earth Obs. Geoinf.*, 34, 51–57.

Phiri, D., Morgenroth, J., Xu, C., 2019. Long-term land cover change in Zambia: An assessment of driving factors. *Sci. Total Environ.*, 134206.

Phiri, D., Simwanda, M., Nyirenda, V., Murayama, Y., Ranagalage, M., 2020. Decision Tree Algorithms for Developing Rulesets for Object-Based Land Cover Classification. *ISPRS International Journal of GeoInformation*, 9(5), 329.

Schöpfer E., Lang S., Strobl J., 2010. Segmentation and Object-Based Image Analysis. In: Rashed T., Jürgens C. (eds) *Remote Sensing of Urban and Suburban Areas. Remote Sensing and Digital Image Processing*, 10. Springer, Dordrecht,Chapter 10.2.1

URL-1 Weather 67.84°S 67.18°W Available online: https://www.meteoblue.com/en/weather/week/67.844N-67.181E0_Antarctica%2FSouth_Pole (accessed on 5 January 2025).

Wang, M., Mao, D., Wang, Y., Xiao, X., Xiang, H., Feng, K., ..., Wang, Z., 2023. Wetland mapping in East Asia by two-stage object-based Random Forest and hierarchical decision tree algorithms on Sentinel-1/2 images. *Remote Sensing of Environment*, 297, 113793.